



HAL
open science

A multifunctional standardized magnetic tunnel junction stack embedding sensor, memory and oscillator functionality

A. Chavent, V. Iurchuk, L. Tillie, Y. Bel, N. Lamard, L. Vila, U. Ebels,
Ricardo C. Sousa, B. Dieny, G. Di Pendina, et al.

► To cite this version:

A. Chavent, V. Iurchuk, L. Tillie, Y. Bel, N. Lamard, et al.. A multifunctional standardized magnetic tunnel junction stack embedding sensor, memory and oscillator functionality. *Journal of Magnetism and Magnetic Materials*, 2020, 505, pp.166647. 10.1016/j.jmmm.2020.166647 . hal-03111526

HAL Id: hal-03111526

<https://hal.science/hal-03111526v1>

Submitted on 23 Apr 2021

HAL is a multi-disciplinary open access archive for the deposit and dissemination of scientific research documents, whether they are published or not. The documents may come from teaching and research institutions in France or abroad, or from public or private research centers.

L'archive ouverte pluridisciplinaire **HAL**, est destinée au dépôt et à la diffusion de documents scientifiques de niveau recherche, publiés ou non, émanant des établissements d'enseignement et de recherche français ou étrangers, des laboratoires publics ou privés.

A multifunctional standardized magnetic tunnel junction stack embedding sensor, memory and oscillator functionality

A. Chavent^a, V. Iurchuk^a, L. Tillie^a, Y. Bel^a, N. Lamard^a, L. Vila^a, U. Ebels^a, R.C. Sousa^a, B. Dieny^a, G. di Pendina^a, G. Prenat^a, J. Langer^b, J. Wrona^b, I.L. Prejbeanu^a

^aUniv. Grenoble Alpes / CEA / CNRS, Spintec, France

^bSingulus Technology, Germany

Abstract

The objective of this study is to co-integrate multiple digital and analog functions together within CMOS by developing a universal magnetic tunneling junction stack (MTJ) capable of realizing logic, memory, and analog functions, within a single baseline technology. This will allow monolithic heterogeneous integration, fast and low-power processing, and high integration density, particularly useful for Internet of Things (IoT) platforms. This unique spintransfer-torque (STT) MTJ is called Multifunctional Standardized Stack (MSS). This paper presents the progress regarding memory, oscillator and sensor functionalities targeted for the technology. We show that a single magnetic stack deposition can be used to obtain these three functionalities on the same wafer.

1. Introduction

The MTJs are mainly used nowadays for non-volatile memory (STT-MRAM) [1, 2, 3, 4], but also as magnetic sensors [5, 6, 7]. These functionalities in principle require application specific stacks. Heterogeneous integration allows to enhance the functionalities involved through gains in Si footprint area, and new design possibilities. Very recently the same magnetic stack was used to achieve different memory specifications [8]. The novelty of our work is to create entirely different functions: a non-volatile memory bit, an RF-oscillator and a magnetic sensor, based on the same deposited stack. To the best of our knowledge this is the first such attempt to achieve these 3 functionalities. The starting point is interfacial perpendicular magnetic anisotropy (PMA) MTJ, which is now the mainstream technology of STT-MRAM. The strategy then consists in reducing the perpendicular anisotropy to find a working trade-off for all 3 functions.

The principle of the heterogeneous integration here is to have a front end CMOS, with back-end MTJs processed into pillars. A current is then sent through the MTJ which induces switching or precessional motion of its magnetization under STT. For sensor operation, magnetic flux concentrators will be integrated around the specific MTJs to be used as sensors. Since the MTJ has perpendicular anisotropy, the flux concentrator will

amplify the in-plane field to exploit reversible magnetization rotation arising when field is applied along the hard axis.

2. Experimental Method

The magnetic stack was developed in a Singulus sputtering tool : [Co 0.5/Pt 0.2]₆/Ru 0.8/[Co 0.6/Pt 0.2]₃/Ta 0.2/Co 0.9/W 0.25/CoFeB 1/MgO 0.8/CoFeB x /W 0.3/CoFeB 0.5/MgO 0.75nm, where $x = 1.3$ nm or 1.4 nm. The reference layer is a compensated synthetic antiferromagnet (SAF). CIPT measurements lead to TMR = 170 % and RA = 7.5 $\Omega\mu\text{m}^2$. The stacks were processed into circular pillars with academic and industrial nanofabrication process flows. At the academic facility, pillars were fabricated using e-beam lithography and ion beam etching (IBE) into diameters from 20 nm to 200 nm, while at the industrial facility they were processed into pillars of diameter 130 nm to 180 nm.

For the characterization of individual MTJ, magneto-resistance measurements were done with a positive voltage bias of 20 mV. In our sign convention, positive current or voltage corresponds to electrons flowing from the reference layer to the storage layer.

3. MTJ process characterization

The basic wafer level MTJ parameters: resistance, TMR, coercive and offset fields are measured with an out-of-plane field sweep at 5 Hz after patterning. 20 MTJs per die are measured, and the resulting yield measurement on a full wafer map is shown on Fig. 1. The die yield is defined as the percentage of MTJs on a die having a TMR value above 70 %, in agreement with design assumptions for this technology. Most dies have yields above 90 %, with about half of the dies having a single junction out of spec, corresponding to 95 % yield.

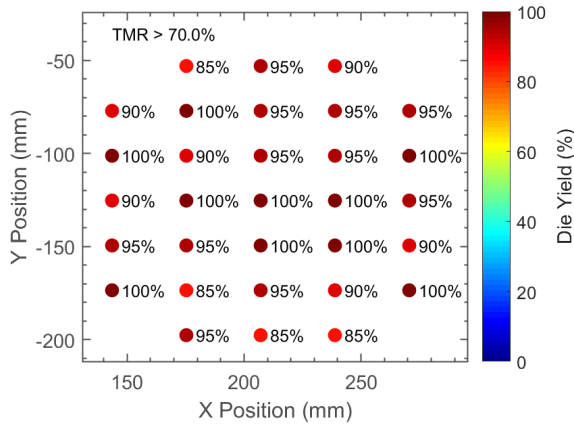


Figure 1: Wafer map of the die yield, defined as the yield of each die for a TMR criteria of 70 %.

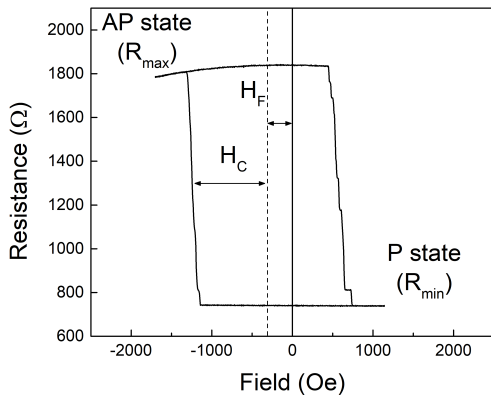


Figure 2: Magnetoresistance loop of the perpendicular MTJ. H_F is the offset field, H_C is the coercive field, R_{min} and R_{max} are respectively the resistance in P and AP state.

4. Memory characteristics

To verify memory operation, we characterized the writing behavior using resistance state phase diagrams on individual test cells. The measurement procedure is as follows: the magnetic field is swept continuously, while applying 100 ns voltage pulses at each magnetic field step. The resistance value is measured at 1000 field points along the recorded hysteresis loop, with a voltage of 20 mV. The pulse voltage is varied from 20 mV to 1 V, for both positive and negative values. The measured resistance state is plotted in a diagram as function of field and pulse voltage in Fig. 3.

At a given field of 200 Oe, the high resistance antiparallel (AP) and low resistance state parallel (P) are reached for pulses of 0.7 V respectively with positive and negative voltages. This shows the memory functionality by STT writing, however it requires an external applied field of 200 Oe, to compensate the dipolar coupling field from the reference layer H_F favoring the P state, as shown in Fig. 2. The coupling field can be reduced by changing the SAF reference layer to provide better field compensation without impacting the writing behavior [9]. A second factor prevents writing at zero field, which is the reduction of coercivity above 0.6 V (Fig. 3). The observed affect, can be related to cell heating at higher voltage thereby reducing the anisotropy of the storage layer or to some storage-reference layer interaction reducing the stability of the written state. In any case the best strategy to achieve zero field operation would be to reduce the reference layer dipolar coupling field.

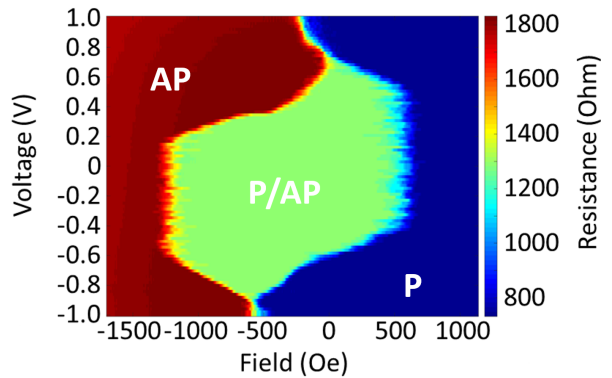


Figure 3: Phase diagram of an MTJ as function of out-of-plane field and voltage amplitude of 100 ns pulses.

To characterize memory retention for operation as a non volatile memory, we also measured the thermal sta-

bility barrier $\Delta = \frac{E}{k_B T}$. The thermal stability is estimated from the switching field distribution [10], obtained from 300 hysteresis loop measurements (Fig. 4). Values of Δ are around 40 to 60, which corresponds to a minimum retention of 10 years for one bit, achieving the design requirements of some applications. Due to the coupling field of the reference electrode H_F , the AP state is less stable, and the reduction of stability can be estimated by including a correction coefficient $(1 - H_F/H_K)^{3/2}$, where H_K is the anisotropy field of the storage layer, in the range 1000 Oe to 2000 Oe. The stability of AP state decreases strongly for H_F/H_C above 0.5, falling below 30, which implies a retention of only a few hours. As previously mentioned, one solution is to reduce the coupling field, however a second option is to increase the coercive field without changing the stack.

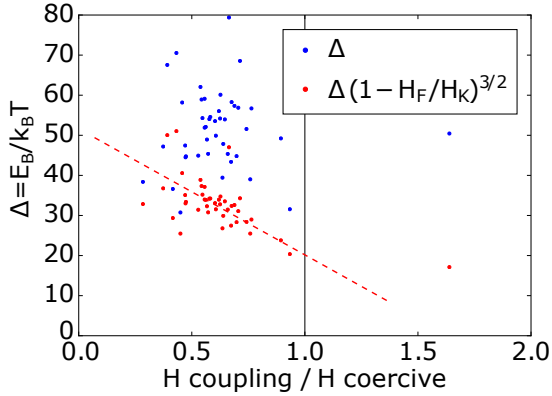


Figure 4: The stability Δ as function of the ration H_F/H_C between the coupling field and the coercive field. $\Delta(1 - H_F/H_K)^{3/2}$ is the stability of the AP state. Δ and H_K are estimated by fitting the switching field distribution.

This can be achieved by reducing the pillar diameter through a trimming process by ion beam etching at a grazing angle. Since the ion beam etch is highly directional, the grazing etch angle increases the pillar lateral etch rate (horizontal etch component), while reducing at the same time the vertical etch rate.

The amount of lateral trimming was controlled through time, using longer etch times to achieve stronger trimming of the patterned pillars. For strong trimming conditions, the cell diameter is confirmed to decrease. This is shown in Fig. 5, where samples having strong trimming show effective pillar diameters that are reduced, compared to short trimming conditions. At the same time the coercive field H_C of the storage layer of smaller cells also increases. One possible explanation for this increase, is that the

magnetization reversal mechanism in interfacial PMA MTJ is the nucleation of a domain wall (DW) at pillar edge and its subsequent propagation [11]. The increase of coercive field through trimming would then result from the reduction of DW nucleation sites on the reduced cell area and circumference.

The increase of coercive field reduces the impact of the reference layer coupling field. In fact, as shown in Fig. 5, the ratio between the coupling field and the coercive field is below one in the case of strong trimming. It means that the trimming only increased the coercive field, but not the coupling field. Having this ratio below one allows zero field operation.

The STT efficiency was calculated assuming $\Delta = 70k_B T$, an average switching voltage of 0.5 V and $RA = 7.5 \Omega \mu m^2$, resulting in $1.5 k_B T / \mu A$ for a 30 nm diameter device, which is about half the efficiency reported for comparable state-of-the-art stacks [10].

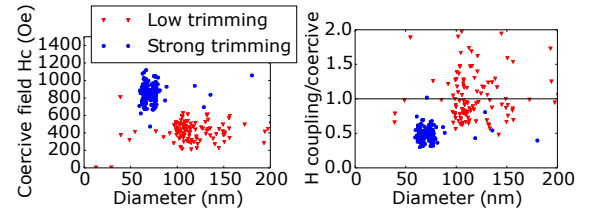


Figure 5: Left : Coercive field. Right : Ratio between coupling and coercive field, which depicts the stability in zero field. The data are shown for low or strong trimming during the IBE etching, as function of diameter calculated from electrical resistance and RA.

5. Sensor functionality

The basic principle for magnetic field sensor operation is for the field to induce a change of the angle α between the reference and the storage/sensing layer magnetization direction. This result in a resistance change the according following relationship [12]:

$$G(\alpha) = \frac{G_P + G_{AP}}{2} + \frac{G_P - G_{AP}}{2} \cos(\alpha) \quad (1)$$

Where $G = 1/R$ is the conductance, R the resistance, G_P and G_{AP} the conductance in the P and AP state.

Various sensor applications exist with their own specific requirements. Here the objective was to have a reversible dependence with low hysteresis, allowing for the measurement of one single magnetic field

component.

To identify field ranges with possible sensor operation, we measured magnetoresistance loops for various angles θ of the field with respect to the easy axis orthogonal to the wafer plane, as shown in Fig. 6. Hysteretic switching of the storage layer along its anisotropy axis is observed at measured field angles below $\theta = 80^\circ$. For $\theta = 45^\circ$, starting in the AP state, the resistance varies reversibly on a range of a few thousand Oersted. This behavior is reversible and corresponds to a first scenario of magnetic sensor functionality. For θ around 85° , the main hysteresis field range disappears, and is replaced by reversible resistance change around the P state, corresponding to a second possible sensing scenario providing larger sensitivity on a narrower range of fields.

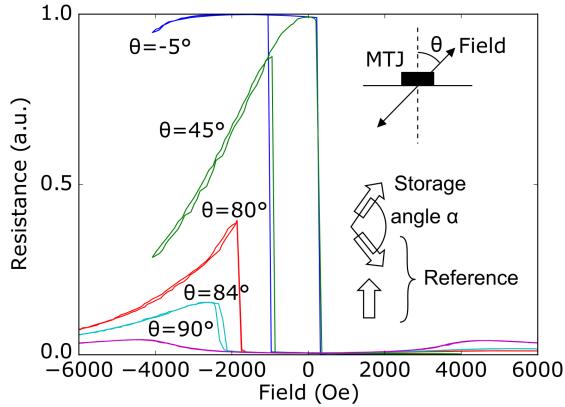


Figure 6: Magnetoresistance loops of a perpendicular MTJ with the stack where the CoFeB thickness x is 1.4 nm. The loops are measured for various angles of the field with respect to the normal to the wafer.

To better understand these behaviors and verify whether further improvements are possible, we made a macrospin energy model, illustrated on Fig. 7. It allows for the calculation of the magnetization angle ϕ of each layer as a function of applied magnetic field. For scenario 1 with $\theta = 45^\circ$, the angle ϕ of the storage layer almost does not change within the sensing field range. The change of resistance through the angle α is mainly due to the rotation of the top part of the reference (Reference 2). For the scenario 2 with $\theta = 84^\circ$, the closest behavior with the same parameters of the model was obtained assuming a field angle of $\theta = 86^\circ$. In that case, the reference layer (Reference 2) slowly rotates on a large field range of a few thousand Oe as previously. However, it is the reversible rotation of the storage

layer around 2000 Oe which is actually responsible for the largest resistance change observed in the second sensing scenario.

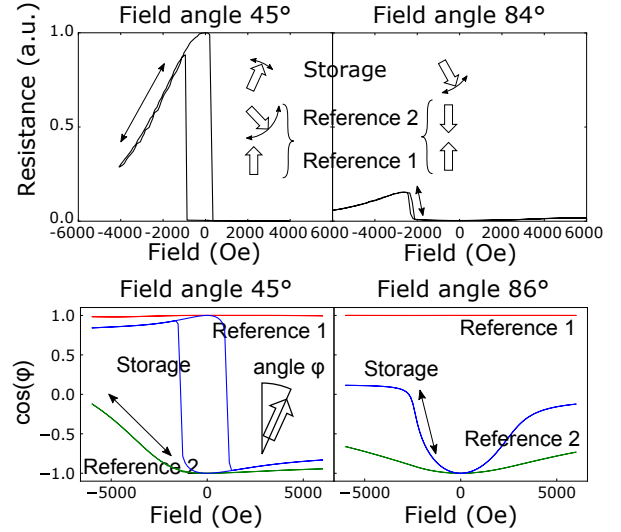


Figure 7: Top : measurement taken from 6. Bottom : angle ϕ of each layer of the stack in a macrospin energy model. Left : scenario 1 with sensing around the AP state. Right : scenario 2 with sensing around the P state.

5.1. Flux concentrator

Magnetic flux concentrators (MFC) were integrated on the MTJs aimed at demonstrating sensor functionality for two reasons. The first is to increase the sensitivity, the second one is to achieve the overlap the operating field window for memory and sensor operation. These flux concentrators are made of electrodeposited NiFe, as shown on Fig. 8. Table 1 summarizes the properties of various flux concentrator geometries fabricated for different values of the thickness and gap.

5.2. Flux concentrator characterization

To characterize the efficiency of the MFC, the in-plane field required to switch the storage layer, as in sensing scenario 2, was compared with and without flux concentrators. The uncertainty associated to this calibration procedure is that the field within the gap of the flux concentrators, at the MTJ level, might be tilted compared to the external magnetic field axis leading to changes in switching field ($\theta = 80^\circ$ and $\theta = 84^\circ$ on Fig. 6). Fortunately, the field tilt is linked to the angle

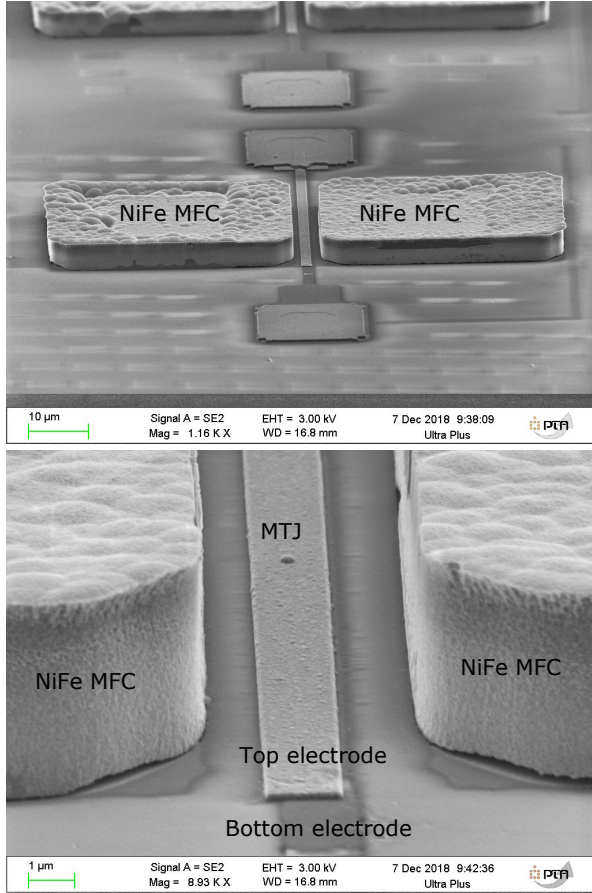


Figure 8: SEM image of the MTJ with MFC integrated.

α , which can be deduced from the magneto-resistance.

The field amplification factor is given in the table 1. The best factor is 6, and is obtained for large Thickness/Gap ratio of 0.9, in agreement with literature [13]. We also made variations of the MFC shape, but differences between them are within the experimental error.

Thickness	2.5 μm	2.5 μm	4.5 μm
Gap	5 μm	11 μm	5 μm
Thickness/Gap	0.5	0.2	0.9
Amplification Factor	3.4	2.3	6

Table 1: MFC characteristics and measured field amplification factor of the MFC integrated MTJ.

5.3. Sensor characterization

The sensor sensitivity of the MTJ with MFC integrated was characterized. In Fig. 9, the magnetoresistance curve with and without MFC are compared.

In the case of an out-of-plane field, the sensing scenario 1 can be applied, showing a reversible change of resistance of the AP state over a field range of 3000 Oe. The sensitivity of this sensing scenario is clearly improved by the use of an MFC. The resulting magnetoresistance loop is similar to that of Fig. 7 without MFC, assuming $\theta = 45^\circ$, even though the external field is applied out-of-plane. This is probably due to a small in-plane field component arising from the flux concentrators. In the case of in-plane field, without MFC, no change of resistance can be seen on the ± 1000 Oe field range. However, using MFC in the sensing scenario 2 configuration, a reversible resistance change of around 500 Oe can be observed. This field value can be compared with the 2000 Oe obtained without MFC (Fig. 7, $\theta = 84^\circ$). The MFC clearly allows to bring the sensor field window closer to the memory working field window.

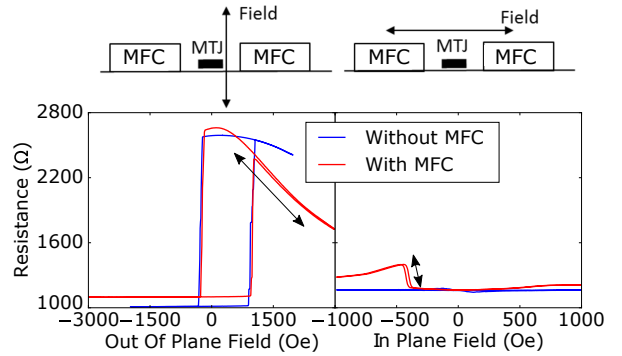


Figure 9: Sensing tests with and without the MFC integrated.

The sensitivity of various samples in both scenarios is summarized in table 3. The sensitivity was measured for a DC bias voltage of 30 mV and estimated at 400 mV by taking into account the dependence of resistance with bias voltage which are give by : $V : R_{AP}/R_{AP0} = 1 - 0.6V$ and $R_P/R_{P0} = 1 - 0.04V$. The sensitivity obtained in the scenario 2 compares well with those of standard dedicated FeCoB/MgO/FeCoB MTJ. For example in reference [7] a sensitivity of 39 V/T is reported on a few tens of Oersted. The main difference in our case is the offset of 500 Oe, that would have to be taken into account for the application. Further examples are discussed in a recent review paper on magnetoresistance (MR) sensors[14], highlighting how different MR technologies can be applied in specific sensing tasks.

	scenario 1	scenario 2
Field angle θ	10 to 20 °	80 to 90 °
Sensitivity	0.05 to 0.08 %/mT 0.15 to 0.25 V/T	1 to 10 %/mT 4 to 40 V/T
Offset	1000 Oe	500 Oe
Range	1500 Oe	50 Oe

Table 2: Sensor characteristics in both scenario. The sensitivity in unit V/T, was estimated with a bias voltage of 400 mV.

	Perpendicular	In-plane
Field angle θ	10 to 45 °	80 to 90 °
Sensitivity	0.05 to 0.08 %/mT 0.15 to 0.25 V/T	1 to 10 %/mT 4 to 40 V/T
Range	1500 Oe	50 Oe

Table 3: Sensor characteristics in both scenario. The sensitivity in unit V/T, was estimated with a bias voltage of 400 mV.

6. Oscillator characteristics

Spin torque oscillators allow for radio frequency (RF) functionality, in a frequency range of 1-20 GHz. Various RF functionalities were explored, such as generation, detection and modulation. For RF generation, as an example, the principle is to apply a DC current to the MTJ, such that it exerts a torque on the storage layer by STT, which will trigger sustained oscillations. These magnetization oscillations yield oscillations of the MTJ resistance which consequently emits an RF current.

For the measurement shown in Fig. 10, an in-plane field is applied, with positive applied current flowing through the MTJ, while the power spectral density (PSD) is measured as a function of the frequency. There is a clear peak in the PSD due to RF oscillation. It appears more clearly with positive current polarity. In fact, as shown in Fig. 6, with an in-plane field, it is not possible to obtain an AP state, and the oscillations appear around the P state resistance level. The positive current is supposed to stabilize the storage layer in the P state instead of triggering oscillations. The more likely explanation is therefore that the reference layer oscillates due to the positive current destabilizing the P state reference layer direction.

The generation was characterized for two configurations, one using in-plane field and the other out-of-plane field. The performance parameters for signal generation are the emission linewidth and the generated output power, that are summarized in table 4 for both field orientations. As can be seen for out-of plane field much

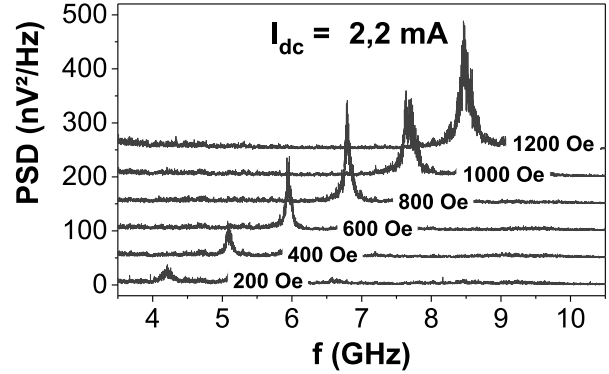


Figure 10: Spectrum of the RF response to a DC current, with in-plane field

better performances were achieved with a linewidth of 20 MHz and a power of 20 nW. These values are in the range in-plane magnetized MTJ devices [15] and will allow testing further functionalities such as injection locking, modulation or insertion into a Phaselocked loop (PLL) for frequency synthesis. Experiments on this are currently ongoing using our previously developed hybrid CMOS-PCB PLL circuit [16].

The frequency, linewidth and power emission are summarized in table 4. It is possible that these two configurations correspond to the sensing scenarios described above. In the configuration of in-plane field, the linewidth 100 MHz is too large, and the power 0.8 nW is too low to allow its use coupled to a phase locked loop (PLL), the basic block of a RF synthesis circuit. On the contrary, with out-of-plane field, the linewidth 20 MHz and the power 20 nW are compatible with PLL requirements.

Field	In-plane 800 Oe	Out-of-plane 2200 Oe
Frequency	5 to 9 GHz	3 to 5 GHz
Linewidth	100 MHz	20 MHz
Power	0.8 nW	20 nW

Table 4: Generation characteristics of the MSS in two magnetic field configurations.

7. Conclusion

We have verified the functionality of storage, field sensing and RF generation of magnetic tunnel junctions fabricated with the same perpendicular MTJ stack. For memory applications, STT writing was confirmed on devices having an energy barrier compatible with 10 year bit retention. Achieving zero field operation still requires a reduction of the reference layer dipolar

coupling field, that can be achieved by reducing the magnetic moment of the thicker Co/Pt multilayer SAF structure. For sensing, two scenarios are possible, one on a large field range with low sensitivity, the other on a narrower field range with high sensitivity. We also report RF generation with characteristics compatible with CMOS integration.

This work has received funding from the European Union's Horizon 2020 research and innovation program under grant GREAT No. 687973 and ERC Advanced Grant MAGICAL No. 669204.

References

- [1] O. Golonzka, J. G. Alzate, U. Arslan, M. Bohr, P. Bai, J. Brockman, B. Buford, C. Connor, N. Das, B. Doyle, et al., Mram as embedded non-volatile memory solution for 22fl finfet technology, in: 2018 IEEE International Electron Devices Meeting (IEDM), 2018, pp. 18.1.1–18.1.4. doi:10.1109/IEDM.2018.8614620.
- [2] S.-W. Chung, T. Kishi, J. W. Park, M. Yoshikawa, K. S. Park, T. Nagase, K. Sunouchi, H. Kanaya, G. C. Kim, K. Noma, et al., 4gbt density stt-mram using perpendicular mtj realized with compact cell structure, in: 2016 IEEE International Electron Devices Meeting (IEDM), 2016, pp. 27.1.1–27.1.4. doi:10.1109/IEDM.2016.7838490.
- [3] Y. J. Song, J. H. Lee, H. C. Shin, K. H. Lee, K. Suh, J. R. Kang, S. S. Pyo, H. T. Jung, S. H. Hwang, G. H. Koh, et al., Highly functional and reliable 8mb stt-mram embedded in 28nm logic, in: 2016 IEEE International Electron Devices Meeting (IEDM), 2016, pp. 27.2.1–27.2.4. doi:10.1109/IEDM.2016.7838491.
- [4] J. J. Nowak, R. P. Robertazzi, J. Z. Sun, G. Hu, J. Park, J. Lee, A. J. Annunziata, G. P. Lauer, R. Kothandaraman, E. J. O'Sullivan, P. L. Trouilloud, Y. Kim, D. C. Worledge, Dependence of voltage and size on write error rates in spin-transfer torque magnetic random-access memory, *IEEE Magnetism Letters* 7 (2016) 1–4. doi:10.1109/LMAG.2016.2539256.
- [5] A. Bocheux, C. Cavoit, M. Mouchel, C. Ducruet, R. Fons, P. Sabon, I.-L. Prejbeanu, C. Baraduc, High sensitivity magnetic field sensor for spatial applications, in: 2016 IEEE Sensors Applications Symposium (SAS), 2016, p. 1–5. doi:10.1109/SAS.2016.7479836.
- [6] M. Mouchel, A. Bocheux, C. Ducruet, P. Sabon, I.-L. Prejbeanu, Y. Conraux, J. Alvarez-Héroult, K. Mackay, C. Baraduc, Noise study of magnetic field sensors based on magnetic tunnel junctions, *Journal of Physics: Conference Series* 903 (2017) 012008. doi:10.1088/1742-6596/903/1/012008.
- [7] M. Dabek, P. Wisniowski, T. Stobiecki, J. Wrona, S. Cardoso, P. P. Freitas, Sensitivity and 3 db bandwidth in single and series-connected tunneling magnetoresistive sensors, *Sensors* 16 (11) (2016). doi:10.3390/s16111821.
- [8] J.-H. Park, J. Lee, J. Jeong, U. Pi, W. Kim, S. Lee, E. Noh, K. Kim, W. C. Lim, et al., A novel integration of stt-mram for on-chip hybrid memory by utilizing non-volatility modulation, in: 2019 IEEE International Electron Devices Meeting (IEDM), 2019, p. (in press).
- [9] S. Bandiera, R. C. Sousa, Y. Dahmane, C. Ducruet, C. Portemont, V. Baltz, S. Auffret, I. L. Prejbeanu, B. Dieny, Comparison of synthetic antiferromagnets and hard ferromagnets as reference layer in magnetic tunnel junctions with perpendicular magnetic anisotropy, *IEEE Magnetism Letters* 1 (2010) 3000204–3000204. doi:10.1109/LMAG.2010.2052238.
- [10] L. Thomas, G. Jan, J. Zhu, H. Liu, Y.-J. Lee, S. Le, R.-Y. Tong, K. Pi, Y.-J. Wang, D. Shen, R. He, J. Haq, J. Teng, V. Lam, K. Huang, T. Zhong, T. Tornig, P.-K. Wang, Perpendicular spin transfer torque magnetic random access memories with high spin torque efficiency and thermal stability for embedded applications (invited), *Journal of Applied Physics* 115 (17) (2014) 172615. doi:10.1063/1.4870917.
- [11] T. Devolder, J. Kim, J. Swerts, S. Couet, S. Rao, W. Kim, S. Mertens, G. Kar, V. Nikitin, Material developments and domain wall-based nanosecond-scale switching process in perpendicularly magnetized stt-mram cells, *IEEE Transactions on Magnetism* 54 (2) (2018) 1–9. doi:10.1109/TMAG.2017.2739187.
- [12] J. C. Slonczewski, Conductance and exchange coupling of two ferromagnets separated by a tunneling barrier, *Phys. Rev. B* 39 (1989) 6995–7002. doi:10.1103/PhysRevB.39.6995.
- [13] X. Sun, L. Jiang, P. Pong, Magnetic flux concentration at micrometer scale, *Microelectronic Engineering* 111 (2013) 77–81. doi:10.1016/j.mee.2013.01.063.
- [14] S. Cardoso, D. C. Leitao, T. M. Dias, J. Valadeiro, M. D. Silva, A. Chicharo, V. Silverio, J. Gaspar, P. P. Freitas, Challenges and trends in magnetic sensor integration with microfluidics for biomedical applications, *Journal of Physics D: Applied Physics* 50 (21) (2017) 213001. doi:10.1088/1361-6463/aa66ec.
- [15] A. Ruiz-Calaforra, A. Purbawati, T. Brächer, J. Hem, C. Murapaka, E. Jiménez, D. Mauri, A. Zeltser, J. A. Katine, M.-C. Cyrille, et al., Frequency shift keying by current modulation in a mtj-based stno with high data rate, *Applied Physics Letters* 111 (8) (2017) 082401. doi:10.1063/1.4994892.
- [16] M. Kreißig, R. Lebrun, F. Protze, K. J. Merazzo, J. Hem, L. Vila, R. Ferreira, M. C. Cyrille, F. Ellinger, V. Cros, et al., Vortex spin-torque oscillator stabilized by phase locked loop using integrated circuits, *AIP Advances* 7 (5) (2017) 056653. doi:10.1063/1.4976337.